© 2009



Springer

www.scichina.com tech.scichina.com www.springerlink.com

Extension of the pressure correction method to zero-Mach number compressible flows

HE YaLing[†], HUANG Jing, TAO YuBing & TAO WenQuan

State Key Laboratory of Multiphase Flow in Power Engineering, School of Energy & Power Engineering, Xi'an Jiaotong University, Xi'an 710049, China

In the present paper, the classical pressure correction method was extended into low Mach number compressible flow regime by integrating equation of state into SIMPLE algorithm. The self-developed code based on this algorithm was applied to predicting the lid-driven cavity flow and shock tube problems, and the results showed good agreement with benchmark solutions and the Mach number can reach the magnitude of as low as 10⁻⁵. The attenuation of sound waves in viscous medium was then simulated. The results agree well with the analytical solutions given by theoretical acoustics. This demonstrated that the present method could also be implemented in acoustics field simulation, which is crucial for thermoacoustic simulation.

thermoacoustic engine, pressure correction method, low Mach number, compressible flow

1 Introduction

The flow inside thermoacoustic engine is a typical low Mach number compressible flow, where the time averaged flow rate approaches zero and the sound wave transmission is purely based on the compressibility of the working fluid. The thermoacoustic engine utilizes the heat transfer between oscillating gas particles and the solid medium by sound waves to achieve the mutual conversion between heat power and acoustic power. Since the sound wave can cause changes of the thermodynamic conditions of the working fluid, the thermoacoustic engine does not need mechanical moving components, such as pistons and crankshafts in conventional compressors and engines. During the past three decades, the thermoacoustic engines have experienced a rapid development of studies. A lot of new structures and new methods have been put forward to improve its performance, and make it more efficient and more convenient for practical application. In addition, numerical simulations have also been adopted to improve our understanding of the characteristics of the complicated process in thermoacoustic engines. However, conventional simulation methods for thermoacoustic engines are based on quasi one-dimensional method and linear approximations, which could not reveal the details of fluid flow and heat transfer processes. Introduction of the computational fluid dynamics (CFD) method into the thermoacoustic engine simulation will provide a powerful research tool for the further development of the thermoacoustic engine.

The numerical methods for fluid flow prediction can be categorized into two groups: density based and pressure based into two groups: density based and pressure based. For the pressure-based approach, methods can be classified into coupled and segregated. Density-based algorithm is traditionally used to deal with high speed compressible flows. With preconditioning it could be extended to low Mach number regime, but with the expense of much longer computation time. Pressure correction method is one of the segregated methods. It can solve low speed flow successfully for the fixed density, or incompressible flow. Many attempts have been

Received January 8, 2009; accepted March 5, 2009

doi: 10.1007/s11431-009-0171-8

[†]Corresponding author (email: <u>yalinghe@mail.xjtu.edu.cn</u>)

Supported by the Key Project of National Natural Science Foundation of China (Grant Nos. 50736005, 50636050)

made to extend this method into the compressible flow regime^[2-5]. However, most of these works were aimed at the compressible flows with Mach number larger than 0.2. The compressible flows occurring in the thermoacoustic engines are of very low speed and their Mach numbers are close to zero. Such compressible flows are called zero Mach number compressible flow.

Computational methods for low Mach number compressible flows are an active research area in recent years [6-9], and the symposium entitled "Mathematical and Numerical Aspect of Low Mach Number Flows" was held in France in 2004. Muller carried out a multiple-time, single-space scale asymptotic analysis of the compressible Navier-Stokes equations and revealed the relationship between velocity and pressure on different scales of time. Nerinckx et al. [11] introduced a new algorithm ranged between coupled and segregated methods, named the coupled pressure and temperature correction algorithm. Its key idea is to separate the flow and acoustic process in computation. During each step of iteration, toward the aim of satisfying continuity equation, both the pressure correction and the temperature correction are considered. The Mach-uniformity of the algorithm was also studied and the computational codes were validated by simulating the flow through transonic nozzle and natural convection in a rectangular cavity. Refs. [7, 12, 13] introduced the preconditioning method, where the characterized sound speed in the governing equation was lowered to the same magnitude as the convection flow speed. Thus, the eigenvalues of all the algebraic equations approach one, which makes them solvable. Munz et al. [14] extended the classical SIMPLE algorithm to weak compressible flows by using multiscale asymptotic expansion to analyze N-S equations and using multiple pressure variant to solve convection flow and acoustic flow. The simulation program was tested by solving lid-driven cavity flow, one-dimensional sound wave attenuation and Kelvin-Helmholtz problem. Schneider et al. [15,16] put forward a multi-step method to extend the classical compressible algorithm to low-Mach number regime. They also pointed out that the difficulty in low-Mach number compressible flow simulation was caused by two problems: dynamic range and signal speed. The dynamic range problem rooted in the oscillating part of pressure. When Mach number approaches zero, this oscillating part decreases to zero too, which leads to a false reflection in numerical results. On

the other hand, when Mach number is near zero, there will be a magnitude difference between convection velocity and sound speed. To capture the flow in both time levels, the computation efficiency will be deteriorated.

Pressure correction method represented by SIMPLEseries algorithm is mature in low speed flow simulation. As stated in ref. [15], the background pressure scaling by a suitable thermodynamic reference value makes it suitable for low Mach number flow simulation. The present work is to validate the possibility of extending the pressure correction method to the near-zero Mach number flow regime. A two-dimensional simulation code will be developed based on the SIMPLE algorithm. Two simulation examples of lid-driven cavity flow with different densities and shock tube flows will be adopted to test the reliability of the method and simulation code. Then, we will step into the computational aero-acoustic regime to solve the sound wave attenuation problem, which is seemingly first in the literature for the simulation of the thermoacoustic problems with the extended SIMPLE-like algorithm.

2 Numerical method

2.1 Governing equations

The governing equations for the steady-state compressible flows are as follows.

Continuity equation

$$\nabla \cdot (\rho \mathbf{v}) = 0. \tag{1}$$

Momentum equation

$$\nabla \cdot (\rho v v) = -\nabla P + \nabla \cdot (\mu \nabla v) + \frac{1}{3} \nabla (\mu \nabla \cdot v). \tag{2}$$

Energy equation

$$\nabla \cdot (\rho \mathbf{v} T) = \frac{1}{c_p} \left\{ \nabla \cdot (k \nabla T) + \beta T \left[\frac{\partial p}{\partial t} + \nabla \cdot (p \mathbf{v}) - p \nabla \cdot (\mathbf{v}) \right] + \mathbf{\Phi} \right\}, \quad (3)$$

where ρ , ν , P and T represent the fluid density, velocity, pressure and temperature, respectively; μ and k are the viscosity and thermal conductivity, respectively; c_p is the specific heat and β is the thermal expansion coefficient, which equals 1/T for ideal gas. In eq. (3), the internal heat source and radiation are neglected and viscous dissipation Φ is given as

$$\Phi = \mu \left\{ 2 \left[\left(\frac{\partial u}{\partial x} \right)^2 + \left(\frac{\partial v}{\partial y} \right)^2 \right] + \left(\frac{\partial u}{\partial y} + \frac{\partial v}{\partial x} \right)^2 - \frac{2}{3} \left(\frac{\partial^2 u}{\partial x^2} + \frac{\partial^2 v}{\partial y^2} \right)^2 \right\}.$$
(4)

Eqs. (1), (2) and (3) can be further represented in a unified form as

$$\nabla \cdot (\rho \mathbf{v} \phi) = \nabla \cdot (\Gamma_{\phi} \nabla \phi) - R_{\phi} + S_{\phi}, \tag{5}$$

where R_{ϕ} and S_{ϕ} represent the source terms caused by pressure and velocity, respectively. In addition, the equation of state for ideal gas is given as

$$\rho = \frac{p}{RT},\tag{6}$$

where R is the gas constant.

2.2 Pressure correction equation

It is well known that the pressure correction equation plays a very important role in the pressure-correction method. In each iterative step, when the intermediate velocities are solved based on the assumed or previous pressure, they may not satisfy the mass conservation condition. Then the pressure-correction equation will be applied to calculating the pressure correction value, which is used to update the fluid velocity so that the updated velocities can satisfy the continuity equation. Moreover, for the low Mach number compressible flow, the accuracy of the pressure correction depends on the interpolation scheme of the density at the control volume faces. In the following presentation the interpolation scheme for interfacial density will first be discussed. In order to obtain a stable and accurate solution algorithm, a hybrid scheme combining the central difference with the first-order upwind is adopted.

$$\rho_e = \alpha_o \rho_e^{\text{CDS}} + (1 - \alpha_o) \rho_e^{\text{UDS}}, \tag{7}$$

where α_{ρ} is a weighting factor, being $0.9-1^{[19]}$. In eq. (7), ρ_{e}^{UDS} is the interfacial density computed by the first-order upwind scheme, which is given as

$$\rho_e^{\text{UDS}} = (0.5 + \omega_e)\rho_P + (0.5 - \omega_e)\rho_E,$$
 (8)

where ρ_p and ρ_E are the density at points P and E, and the weighting coefficient ω is

$$\omega = \begin{cases} 0.5, & F \ge 0, \\ -0.5, & F < 0, \end{cases}$$
 (9)

where F is the interface flux, ρ_{e}^{CDS} is the interfacial

density at *e* interface computed by the central difference scheme, which is given by

$$\rho_{\varrho}^{\text{CDS}} = f_{\varrho}^{-} \rho_{P} + f_{\varrho}^{+} \rho_{E}, \tag{10}$$

with f_e^+ , f_e^- being the interpolation factors.

Moreover, the density corrections at the interfaces, i.e., $(\rho')_e^{\text{UDS}}$ and $(\rho')_e^{\text{CDS}}$ in these two numerical schemes, are given respectively as

$$(\rho')_{\rho}^{\text{UDS}} = (0.5 + \omega_{\rho})C_{P}^{\rho}p_{P}' + (0.5 - \omega_{\rho})C_{E}^{\rho}p_{E}', \quad (11)$$

$$(\rho')_e^{\text{CDS}} = f_e^- C_P^\rho \rho_P' + f_e^+ C_P^\rho \rho_E', \tag{12}$$

where C_P^{ρ} , C_E^{ρ} are transformation factors between density and pressure for grid points P and E, respectively. Obviously for the ideal gas, we have $C^{\rho} = 1/(RT)$.

Now, attention is turned to the derivation of pressurecorrection equation. The discretized continuity equation is

$$(F_e - F_w)\Delta y + (F_n - F_s)\Delta x = 0, \tag{13}$$

where the interface flow rate at e-interface is

$$F_{\rho} = (\rho_{\rho}^* + \rho_{\rho}')(u_{\rho}^* + u_{\rho}')\Delta y. \tag{14}$$

Similar expressions can be written for the other interface flow rates.

The pressure correction equation can be obtained from eq. (13) by substitutions of the related expressions of ρ' via p'

$$\frac{a_P}{\alpha_P} p_P' = \sum a_{\rm nb} p_{\rm nb}' + b, \tag{15}$$

where p'_P and p'_{nb} represent pressure correction at P point and neighboring points. b is the source term, a_P is the coefficient of grid point P, which is given as

$$a_{P} = [\rho_{e}^{*}d_{e} + \rho_{w}^{*}d_{w} + (0.5 + \lambda_{e}^{-})c_{P}^{\rho}u_{e}^{*} - (0.5 - \lambda_{w}^{+})c_{P}^{\rho}u_{w}^{*}]\Delta y + [\rho_{n}^{*}d_{n} + \rho_{s}^{*}d_{s} + (0.5 + \lambda_{n}^{-})c_{P}^{\rho}v_{n}^{*} - (0.5 - \lambda_{s}^{+})c_{P}^{\rho}v_{s}^{*}]\Delta x,$$
 (16)

and $a_{\rm nb}$ is the coefficients of neighboring grid points.

Taking point E as an example, the coefficient a_E is

$$a_F = [\rho_e^* d_e - (0.5 - \lambda_e^+) c_F^\rho u_e^*] \Delta y.$$
 (17)

The underrelaxation factor α_P ranges from 0.8 to 1.0. It should be pointed out that the final convergent results are independent of α_P .

In eqs. (16) and (17), the coefficients λ and d, e.g., at interface e, are defined as

$$\lambda_e^+ = \omega_e + 0.5\alpha_P - \alpha_P \omega_e - \alpha_P f_e^+, \tag{18}$$

$$\lambda_e^- = \omega_e - 0.5\alpha_P - \alpha_P \omega_e + \alpha_P f_e^+, \tag{19}$$

$$d_e = \frac{A_e}{a_e}. (20)$$

The pressure and density are corrected by

$$p_{P} = p_{P}^{*} + p_{P}', (21)$$

$$\rho_P = \rho_P^* + \rho_P'. \tag{22}$$

From eqs. (16) and (17), it can be seen that the pressure correction equation has a close relationship with the interpolated density. So the accuracy of the pressure correction depends on the interpolation scheme of the density at the control volume faces.

The solution procedure for one iterative level can be summarized as follows.

- 1) Initialize the velocity and pressure field, denoted by u^0 , v^0 and p^0 .
- 2) Calculate the coefficients and source term of the discretized momentum equations.
- 3) Solve the momentum equations based on the specified pressure field to get the intermediate solution, denoted by u^* and v^* .
- 4) Based on u^* and v^* , solve the pressure-correction equation to get p'.
- 5) Based on the p', recalculate the velocity to get u^{**} and v^{**}

$$u_e^{**} = u_e^* + u_e' = u_e^* + d_e(p_P' - p_E'),$$

$$v_n^{**} = v_n^* + v_n' = v_n^* + d_n(p_P' - p_N').$$

- 6) Solve other variables based on the u^{**} , v^{**} and p^{*} , such as temperature T^{*} .
- 7) Return to step 2, treating u^{**} , v^{**} and p^{*} as the initial velocity and pressure field. Iterate until convergence is reached.

The above discussion set forth the back ground of the present paper. Because our final goal is to simulate the transient process in the thermoacustic engine, the code developed has two modes: steady and unsteady. For the unsteady simulation the solution process for the steady problem described above just consists of one time step forward. And the evolution on the time scale is conducted by full implicit scheme for the stability of solution procedure.

3 Results and discussion

3.1 Lid-driven cavity flow

The physical model for a two-dimensional lid-driven

cavity flow is shown in Figure 1. The lid-driven flow was used as a classical benchmark case for incompressible flow problem. However, in the present paper, in order to validate our code we used the developed compressible code to solve this problem.

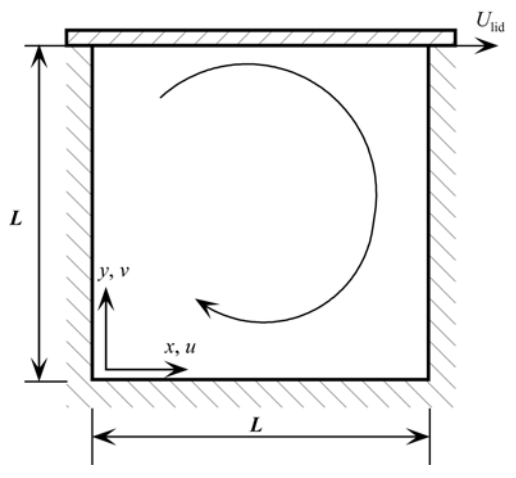


Figure 1 Physical model for the two-dimensional lid-driven cavity flow.

For this case we used the unsteady mode of the code to simulate the steady state problem. At the start of the simulation, fluid in the cavity was set to be still. After the moving of the lid the fluid would move with it because of the effect of the viscosity. When the computational time was long enough, the flow would enter a steady state. In all the cases studied the dimensionless time was long enough to reach a steady state.

In order to compare with benchmark solutions, three Reynolds numbers (100, 1000 and 5000, respectively) were tested. The definition of *Re* is

$$Re = \frac{U_{\text{lid}}L}{v}.$$
 (23)

Dimensionless time is defined as

$$\tau = \frac{U_{\text{lid}}}{L}t. \tag{24}$$

A 102×102 staggered grid was adopted after the independency validation. Figure 2 shows the variation of streamlines with time for *Re*=1000. With the increase of the time, the influence region of the lid expanded. Then the vortices at the lower right corner and the lower left vortex gradually took their shape in order and approach their final patterns. It was found that after the dimensionaless time beyond 30 the flow patterns hardly changed.

Figure 3 shows the steady state streamline at Re=100 and Re=5000, respectively. They agree well with the results of Ghia et al. [17] as shown in Figure 4.

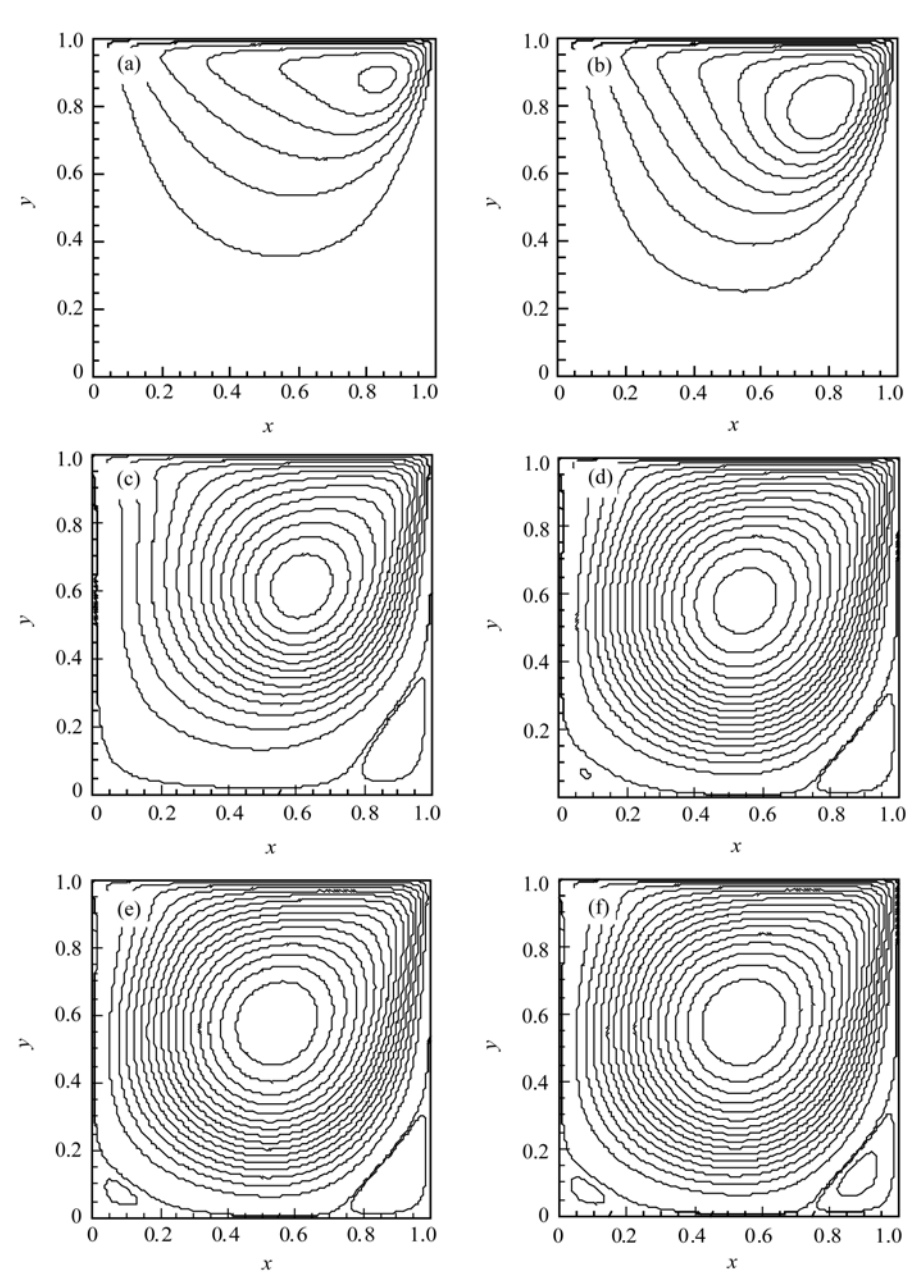


Figure 2 Variation of stream line with time (*Re*=1000). (a) τ =7.694; (b) τ =1.539; (c) τ =4.616; (d) τ =11.540; (e) τ =19.234; (f) τ =26.928.

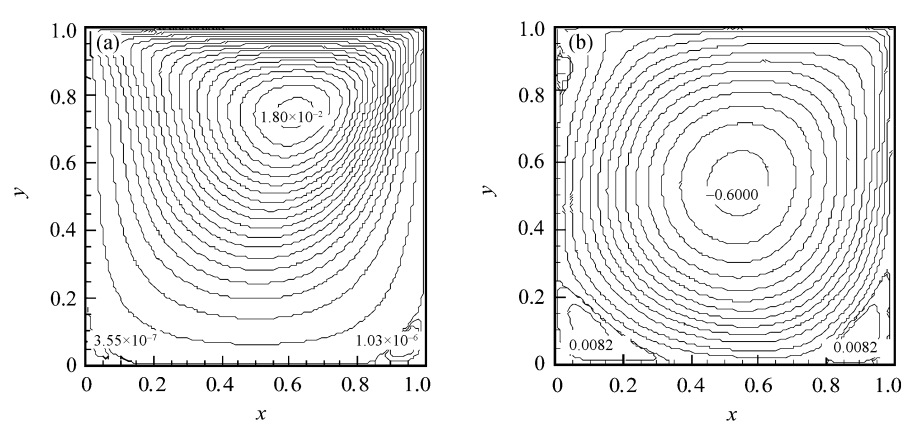


Figure 3 Streamline with different *Re*. (a) *Re*=100; (b) *Re*=5000.

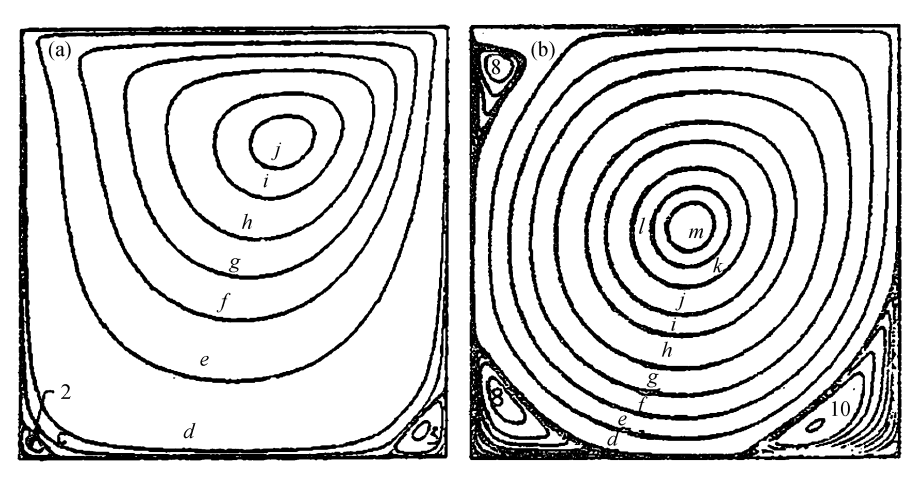


Figure 4 Streamline shown in ref. [17]. (a) *Re*=100; (b) *Re*=5000.

To get a quantitative comparison, the dimensionless velocity U along the centerline of x direction and V along the centerline of y direction were examined. Figure 5 shows the comparison with the results from ref. [17]. Obviously, when Re is low, the agreement is very well. When Re is high, there exists a little difference. This might be caused by the fact that the present results are obtained by a compressible algorithm.

The results of this example show that a low speed flow could be simulated by using the compressible SIMPLE algorithm. In the next step, the program will be used to solve a shock tube problem. By decreasing the pressure difference in the tube, the low Mach number characteristics of the present method will be validated.

3.2 Shock tube

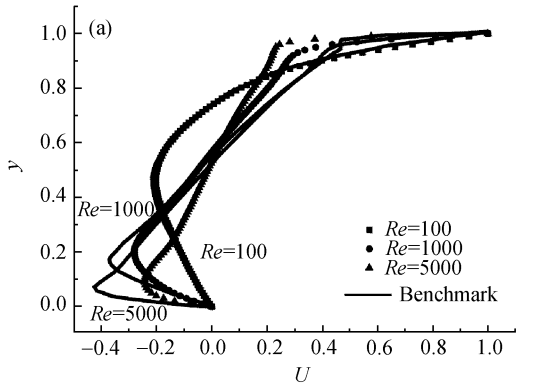
3.2.1 Introduction. Shock tube problem describes the propagation of shock wave in a one-dimensional tube with infinite length. Since there is an exact time-dependent solution for this problem, it is often used as a test case for compressible simulation codes, especially

for shock capturing schemes. In the present work, the pressure difference in it is decreased to form a low Mach number situation. Figure 6 is the schematic for this problem. The initial conditions are expressed as

$$\begin{cases} u/u_0 = u_L = 0, \, p/p_0 = p_L, \, \rho/\rho_0 = \rho_L, \, 0 < x/L_0 < 0.5, \\ u/u_0 = u_R = 0, \, p/p_0 = p_R, \, \rho/\rho_0 = \rho_R, \, 0.5 < x/L_0 < 1, \end{cases}$$
(25)

in which, u_0 , p_0 , ρ_0 , L_0 are characteristic velocity, pressure, density and length, respectively; p_L , ρ_L , p_R , ρ_R are dimensionless initial values.

When the gas at high-pressure flows through the tube into the low-pressure part, shock wave will form at the interface and rarefaction wave will come forth inside the high-pressure part. Between the two waves, there exists a contact discontinuity, where density presents a jump. Mathematically, shock tube problem is a special case for Riemann problem, which has exact solutions. In the present paper, the exact solution gained by the program provided in ref. [18] will be used to validate the numerical results gained by the current simulation code.



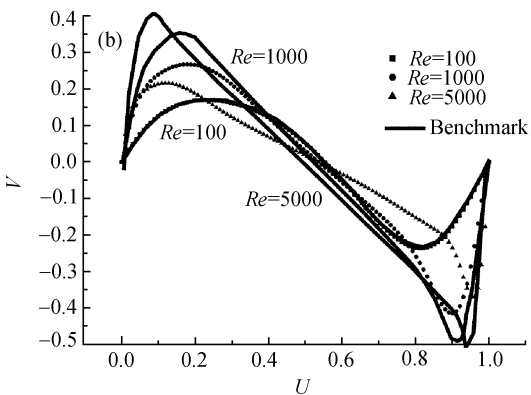


Figure 5 Velocity distribution along centerline. (a) Distribution of U along the line x=0.5; (b) distribution of V along the line y=0.5.

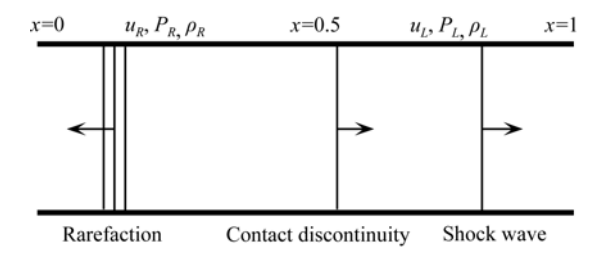


Figure 6 Physical model for shock tube.

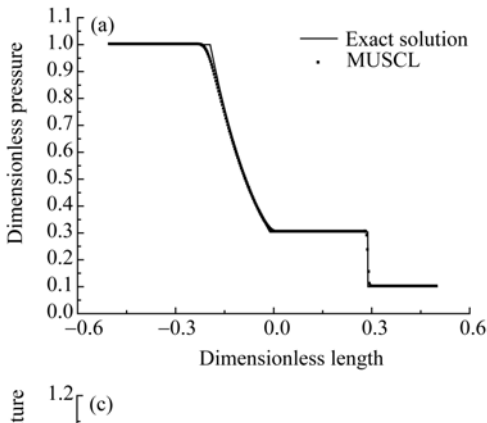
3.2.2 Sod's shock tube model. At first, the Sod's shock tube model will be adopted. Its initial conditions are expressed as

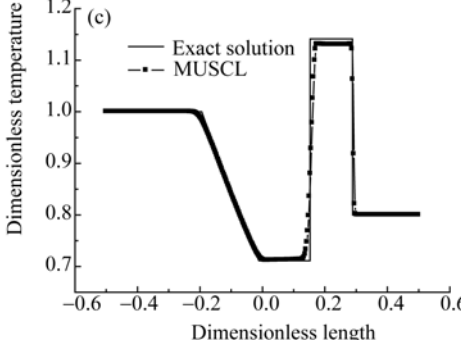
$$\begin{cases} p_L = 1, & \rho_L = 1, \\ p_R = 0.1, & \rho_R = 0.125. \end{cases}$$
 (26)

The aim of the problem is to get the distribution of velocity, pressure, temperature and density at the dimensionless time of 0.1644.

To simulate one-dimensional inviscid flow with our two-dimensional viscous code, we set the viscosity of fluid to zero and implemented a periodical boundary condition at the direction perpendicular to the flow

$$\begin{cases} u(i,1) = u(i, M 2), \\ u(i, M 1) = u(i, 2), \\ v(i, 2) = v(i, M 2), \\ v(i, M 1) = v(i, 3). \end{cases}$$
(27)





By doing so, the length of computational domain at *y* direction will not influence the final result, which means we can simulate a one-dimensional problem with a two-dimensional code.

A 362×17 staggered grid is adopted for the simulation. MUSCL scheme is implemented by using NVD methodology^[7,20]. The results are shown in Figure 7. It can be seen clearly that our numerical results agree well with the exact solution. With MUSCL scheme, the grid number over the shock wave is about four.

3.2.3 Low Mach number shock tube. In the Sod's model, although the fluid is still initial, the final velocity is high. Figure 8 shows the Mach number distribution in Sod's model, the highest Mach number reaches 0.93. However, the focus of our work is for the low Mach number flow. Therefore, we changed the initial pressure difference to lower the Mach number and test the feasibility of our simulation code.

Three conditions with p_L/p_R at 0.9, 0.99 and 0.999 respectively were calculated. The other parameters remained the same as the Sod's model. Since at the time of 0.1644, the pressure wave would reach the end of the computational region and bounce back, to avoid this, we calculated the results at the time of 0.115.

The results are shown in Figure 9. When p_L/p_R is 0.9999, which means a very slight pressure difference,

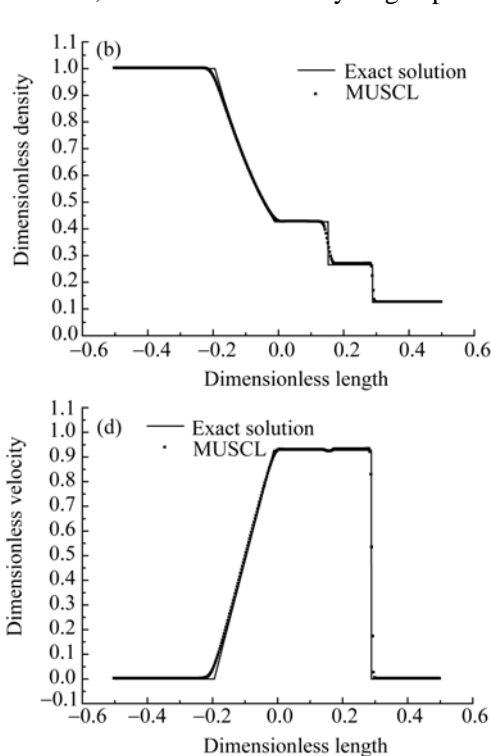


Figure 7 Solution for Sod's shock tube model. (a) Dimensionless pressure; (b) dimensionless density; (c) dimensionless temperature; (d) dimensionless velocity.

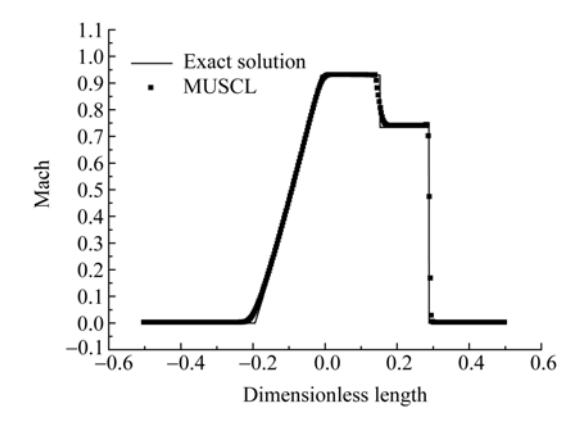


Figure 8 Mach distribution in Sod's model.

the maximum Mach number is as low as 6×10^{-5} . The results show that the discrepancy between our numerical predictions and the exact solutions are very small, which may be caused by some numerical error.

It should be pointed out that we also used first order upper difference (FUD) scheme in these cases. From the comparison results, we can see that its result is almost the same as that of MUSCL, which means that higher order scheme shows little advantage to lower order scheme in low Mach number regime when the grid number is large enough.

3.3 Plane sound wave attenuation

By foregoing work, we proved that the compressible SIMPLE algorithm and the developed code of the present work could be applied to the low Mach number compressible flow. In this part, it will be used to solve an aero-acoustic problem, the attenuation of sound wave in viscous medium.

3.3.1 Introduction. The shock tube was treated as a one-dimensional inviscid problem in the above paragraphs. However, actual fluids are all viscous. When sound waves transmit in them, the sound waves will be attenuated, which means a transfer between acoustic power and heat. This process is called sound wave attenuation. Many factors lead to attenuation, such as viscous force, heat conduction and relaxation effects of molecules. In our work, we only consider the viscous effect. This process is more close to thermoacoustic phenomena compared with those flows encountered in common fluid dynamics and heat transfer.

In theoretical acoustics, the research on sound wave attenuation starts from the one-dimensional wave equation

$$\rho_0 \frac{\partial^2 \xi}{\partial t^2} = K_s \frac{\partial^2 \xi}{\partial x^2} + \eta \frac{\partial^3 \xi}{\partial x^2 \partial t}, \tag{28}$$

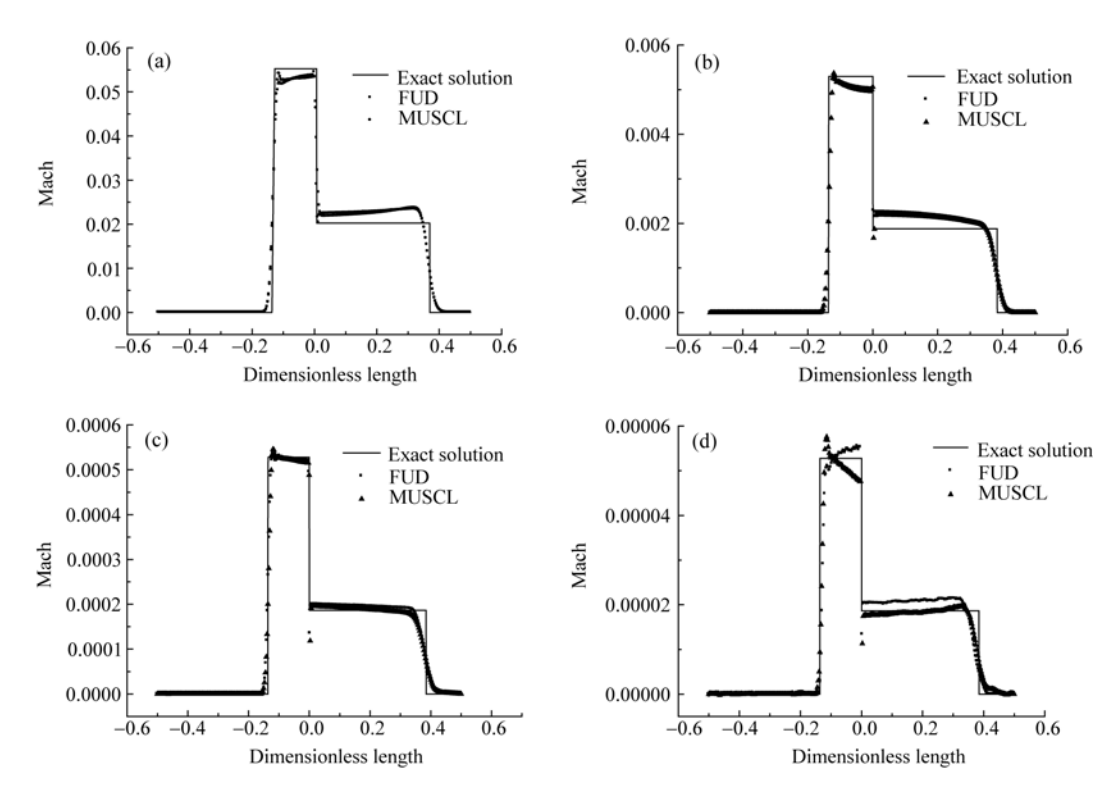


Figure 9 Mach distribution in low Mach number condition. (a) $p_L/p_R=0.9$; (b) $p_L/p_R=0.99$; (c) $p_L/p_R=0.999$; (d) $p_L/p_R=0.9999$.

where K_s is the adiabatic elasticity. For idea gas, $K_s = \gamma P_0$. η is the viscosity, which consists of two parts: shear viscosity η' and volume viscosity η'' .

$$\eta = \frac{4}{3}\eta' + \eta''. \tag{29}$$

By solving eq. (28), the displacement ξ at any place in the sound wave can be expressed as [8,21]

$$\xi = Ae^{-\alpha_{\eta}x}\sin\omega\left(t - \frac{x}{c}\right) + Be^{-\alpha_{\eta}x}\sin\omega\left(t + \frac{x}{c}\right). \quad (30)$$

The first part in eq. (30) stands for a harmonic sound wave propagating to the x^+ direction with a velocity of c and angle frequency of ω . Its amplitude is $Ae^{-\alpha_{\eta}x}$, in which A is decided by the source and $e^{-\alpha_{\eta}x}$ shows an exponential decay of magnitude with the increase of distance from the source. α_{η} is named acoustic absorption coefficient. The second part stands for propagation to the x^- direction, which will be ignored here.

Accordingly, we can get the local velocity [9]

$$u(x,t) = Ue^{-\alpha_{\eta}x}\sin(\omega t - kx), \qquad (31)$$

where k is named wave vector and $k = 2\pi/\lambda$.

When the viscosity is far smaller than the elastic force, the absorption will be very small in one wavelength. In this situation, the absorption coefficient can be expressed as

$$\alpha_{\eta} = \frac{\omega^2 \eta}{2\rho_0 c^3} = \frac{\omega^2}{2\rho_0 c^3} \left(\frac{4}{3} \eta' + \eta'' \right). \tag{32}$$

In our case, the volume viscosity is ignored, which leads to

$$\alpha_{\eta} = \frac{\omega^2 \eta}{2\rho_0 c^3} = \frac{2\omega^2}{3\rho_0 c^3} \eta'.$$
 (33)

Eq. (33) shows that the absorption coefficient is proportional to the square of the frequency in the condition of low viscosity and low frequency. This means that low-frequency sound wave can travel farther than higher ones. At the same time, the greater the fluid viscosity, the higher the absorption coefficient is.

Eq. (33) shows that the absorption coefficient is proportional to the square of the frequency in the condition of low viscosity and low frequency. This means that low-frequency sound wave can travel farther than higher ones. At the same time, the greater the fluid viscosity, the higher the absorption coefficient is.

When the sound wave transmits in confined space,

such as between two parallel plates, the friction between gas and fixed plate will also lead to attenuation. Taking account of this factor, the acoustic absorption coefficient will be larger than that of the one-dimensional problem.

3.3.2 Physical model. The computational region is shown in Figure 10. Sound source is placed at the location of x=0. The source is simulated by a oscillating velocity $u_0 = U \sin(\omega t)$, in which U is the magnitude of velocity oscillating and equals 1.058×10^{-4} m/s, ω is the angle frequency. Mean pressure is 101325 Pa.

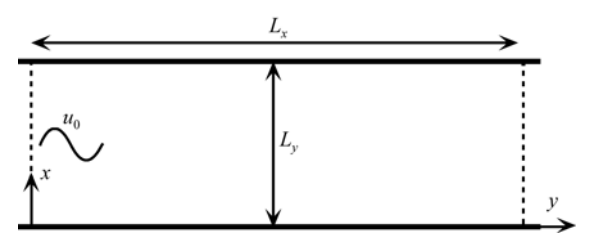


Figure 10 Physical model for sound wave attenuation problem.

3.3.3 Numerical method and boundary condition. For the one-dimensional problem studied, L_x equals 1.7018 m and L_y equals 1.824 m. L_y is set to be a large number to decrease the influence of boundaries. At the same time, periodical boundary condition is implemented on the upper and lower sides, which is the same as stated in Section 3.2. For the two-dimensional problem, L_x equals 1.7018 m and L_y equals 1.824×10^{-2} m. Non-moving boundary condition is implemented on the upper and lower sides.

In comparison with the problem solved in Section 3.2.2, the main difference in this problem is the boundary condition at the sound source. In the lid-driven flow and shock tube, all the boundaries are solid walls, where u and v are set to be zero. But in this case, a sound source is located on the left side open, which is simulated by setting $u_0 = U \sin(\omega t)$. At this position, all the other unknown parameters, such as pressure, density, are obtained by extrapolation. By doing this, the flow in the chamber is no longer unilateral but an oscillating one, which is different from the traditional problems encountered in conventional flow simulations.

The right side opening remains a fixed solid wall. And the propagation time will be controlled to avoid reflecting on this wall. Since we only consider the attenuation caused by viscosity, the energy equation (temperature equation) will not be solved. After the examination of the grid-independency a 362×42 staggered

grid is adopted.

3.3.4 Results and discussion

3.3.4.1 One-dimensional attenuation

(I) Influence of viscosity

First, a low order scheme (FUD) is used to solve the problem. With an ordinary viscosity of air, $\mu = 1.81 \times 10^{-5}$ Pa·s, the attenuation process is very slow, which costs very long time for the computation. Therefore, we use three large viscosities in our simulation, $10^3 \times \mu$ gam, $10^4 \times \mu$ and $2.5 \times 10^4 \times \mu$.

Figure 11 shows the velocity distribution along the propagation direction with the frequency of 3040 Hz. The dashed lines are the results derived from eqs. (31) and (33). Obviously, our results agree well with the predictions of theoretical acoustics. At the front of the sound wave, there is some deviation, which might be caused by the solid wall boundary at the end of the simulation region. Comparing Figures 11(a), (b) and (c), it could be derived that with the increase of viscosity, the attenuation can be intensified.

The attenuation process will lead to Reynolds stresses [10,22], which will cause second order pressure

gradient p'. It has an analytical expression of

$$p' = -2\rho_0 \left\langle u \frac{\partial u}{\partial x} \right\rangle = \rho_0 \alpha U^2 e^{-2\alpha x}.$$
 (34)

From the simulation results, we can also get this second order pressure gradient, which is shown in Figure 12. The second order pressure gradient is also distributed exponentially, and the results agree well with the analytical solution.

We also tried to use the MUSCL in our simulation (Figure 13). The results show very little difference from Figure 11. Because this problem is still in linear acoustics regime, low order scheme can already get a satisfied result when the grid number is enough.

(II) Influence of frequency

To get the influence of frequency, the one-dimensional attenuation is simulated with two different frequencies. The viscosity is the same, $\mu \times 25000$. The results are shown in Figure 14. Obviously, with the same sound source and medium, high frequency sound wave attenuates more rapidly. This means that low frequency sound wave has a stronger penetration ability, which is in accordance with physical facts.

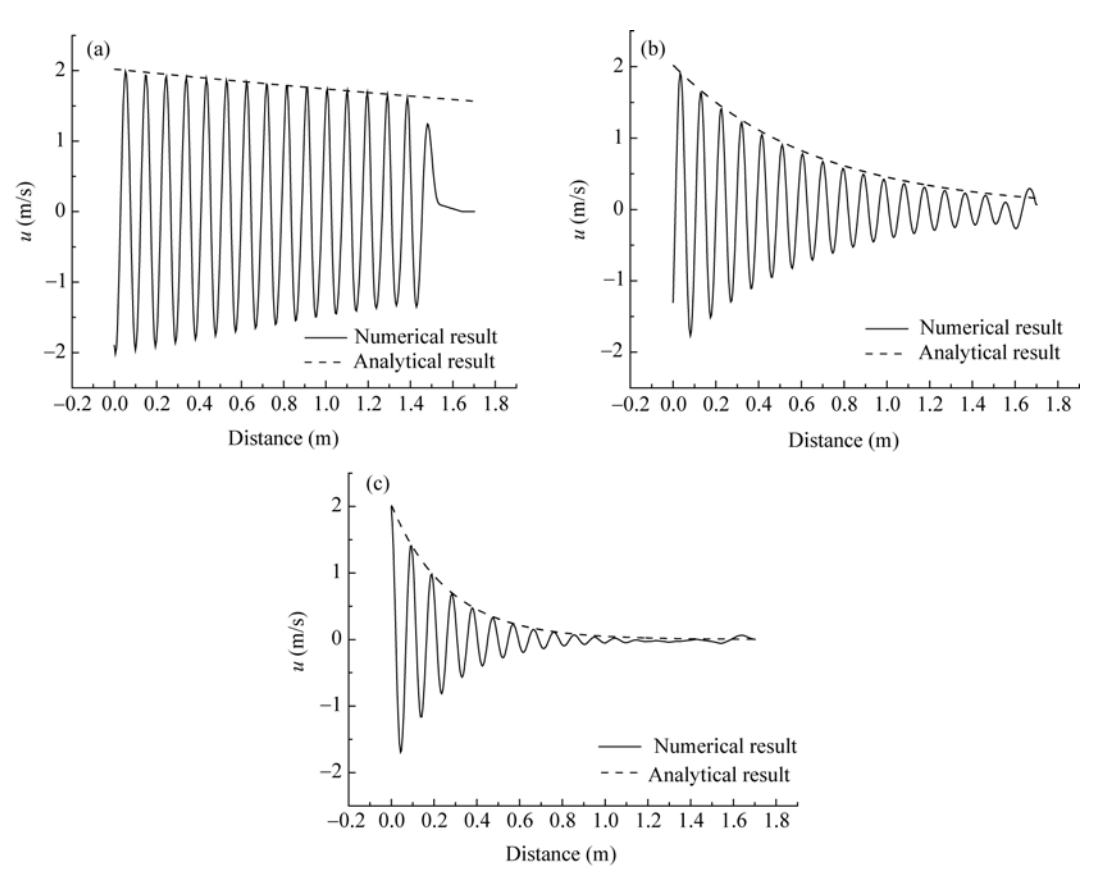


Figure 11 The one-dimensional attenuation with different viscosity (FUD). (a) gam×1000; (b) gam×10000; (c) gam×25000.

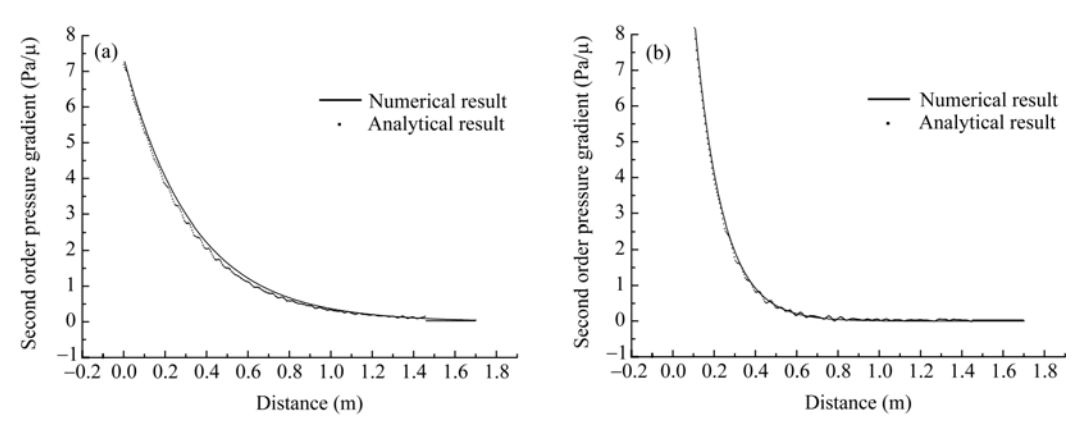


Figure 12 The second-order pressure gradient. (a) gam×10000; (b) gam×25000.

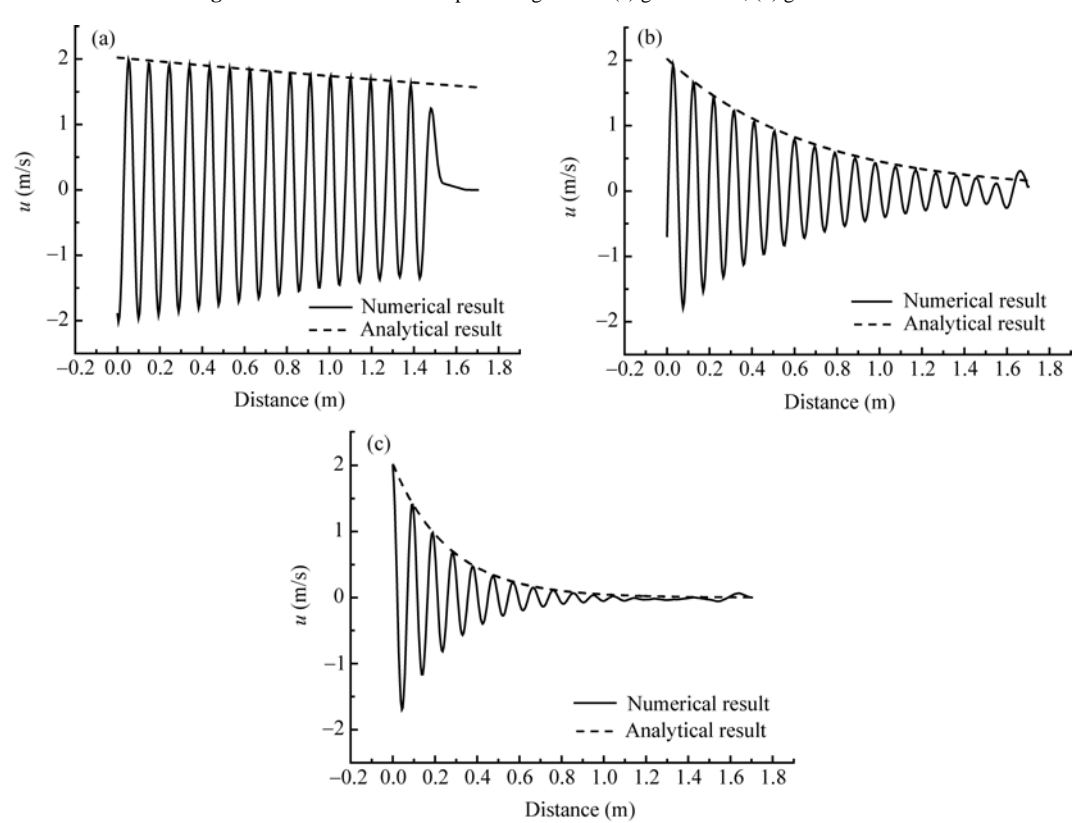


Figure 13 One-dimensional attenuation with different viscosity (MUSCL). (a) gam×1000; (b) gam×10000; (c) gam×25000.

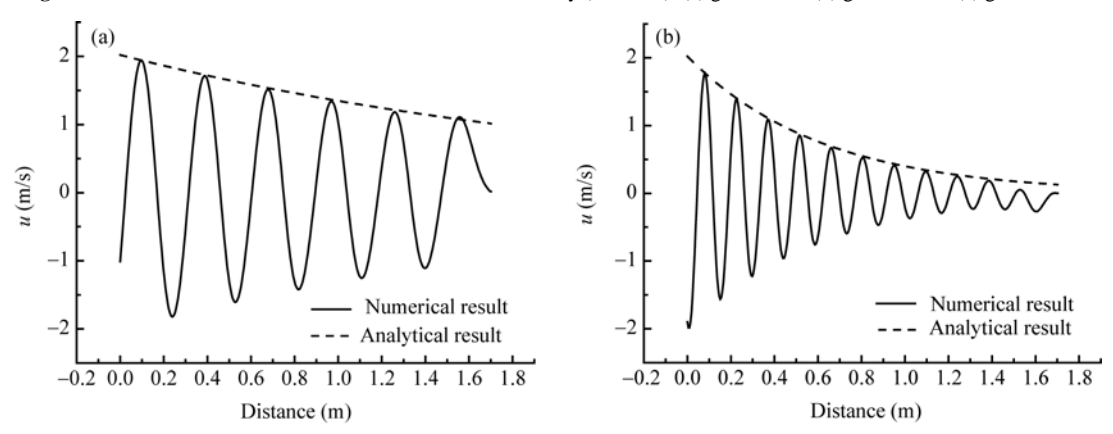
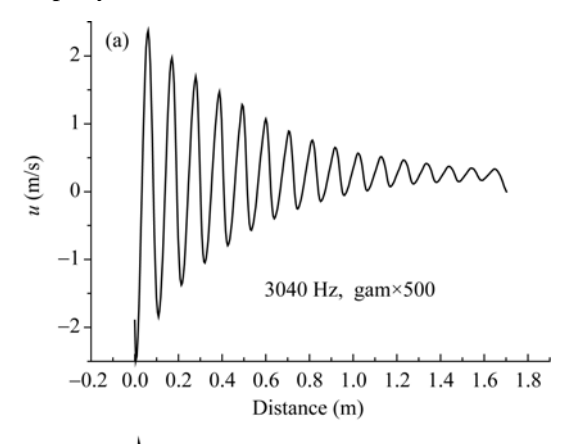


Figure 14 One-dimensional attenuation with different sound source frequency. (a) 1000 Hz; (b) 2000 Hz.

3.3.4.2 Two-dimensional attnuation

As stated before, because of the fixed solid wall, absorption factor for the two-dimensional problem will be larger than that of the one-dimensional problem. Figure 15 shows the velocity distribution along x^+ direction in a two-dimensional attenuation process. The sound source and gas viscosity in Figure 15(b) is the same as that in Figures 11(b) and 13(b). Comparing the three figures, it is clear that in a confined space, the sound wave attenuates more rapidly.



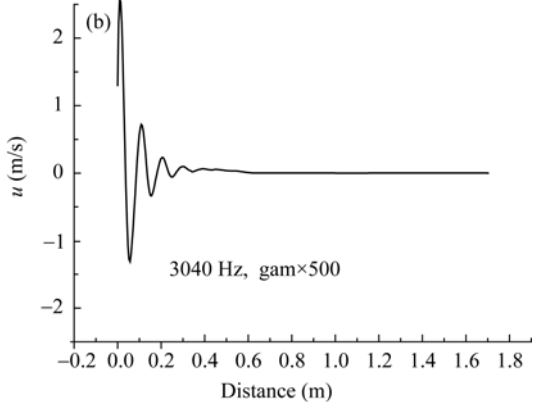


Figure 15 Two-dimensional attenuation with different viscosity (f = 3040 Hz). (a) gam×500; (b) gam×10000.

The influence of solid wall on the sound wave takes place in y direction. In addition to the distribution of u velocity along x direction, its distribution along y direction is also interesting which is shown in Figure 16 in one period. From Figure 16, it can be seen that a viscous boundary layer is near the wall, with a thickness of 2.5-4 mm (this is larger than that in ordinary air, because of a larger

1 Tao W Q. Numerical Heat Transfer (in Chinese). 2nd ed. Xi'an: Xi'an Jiaotong University Press, 2001

2 Van Doormaal J P, Raithby G D, McDonald B H. The segregated ap-

viscosity.). In this layer, the u velocity changes dramatically, from 2 m/s to zero. At the same time, the distribution is not parabolic as in classical flow. At the outside of the boundary layer, there exists a maximum velocity. At the farther place, the velocity is lower and distributes uniformly. This means not only a magnitude difference along the y direction, but also a phase difference.

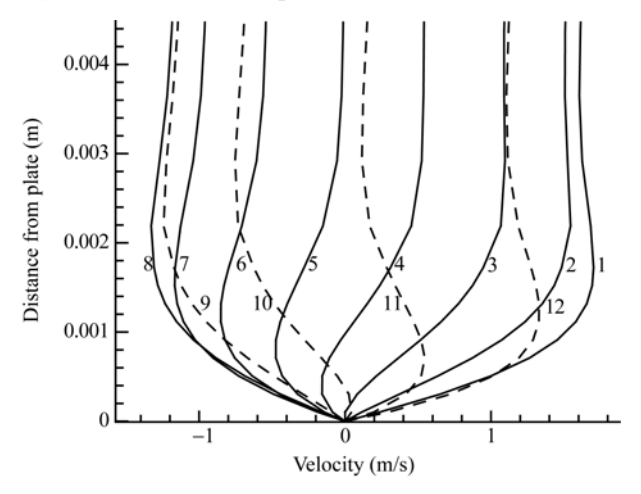


Figure 16 Distribution of *u* velocity along *y* direction in a period.

4 Conclusion

In order to perform the numerical simulation for low Mach number compressible flows (such as the one in thermoacoustic engines), we integrated the equation of state for ideal gas into the classical SIMPLE algorithm and extended the incompressible method into compressible regime. Through two computational examples, liddriven cavity flow and low-Mach number shock tube problem, the feasibility of the method for low Mach number compressible flow is validated. The Mach number in the flow can reach the magnitude of as low as 10^{-5} with reasonable accuracy. The attenuation of sound waves in viscous medium is simulated with an oscillating velocity at the inlet boundary as sound source. The results show good agreement with solutions from theoretical acoustics and classical thermoacoustics, which verifies the feasibility of our method in computational aeroacoustics. The present work establishes a platform for the next attempts to analyze thermoacoustics phenomena based numerical simulation.

proach to predicting viscous compressible flows. ASME J Turbomach, 1987, 109: 265—277

³ Karki K C, Patankar S V. Pressure based calculation procedure for

- viscous flow at all speeds in arbitrary configurations. AIAA J, 1989, 27(9): 1167—1174[DOI]
- 4 Shyy W, Chen M H, Sun C S. Pressure-based multigrid algorithm for flows at all speeds. AIAA J, 1992, 30(11): 2660—2669[DOI]
- 5 Date A W. Solutions of Navier-Stokes equations on non-staggered grid at all speeds. Numer Heat Tr B-fund, 1998, 33(4): 451— 467[DOI]
- 6 Alazard T. Low Mach number limit of the full Navier-Stokes equations. Arch Ration Mech An, 2006, 180(1): 1-73[DOI]
- 7 Birken P, Meister A. Stability of preconditioned finite volume schemes at low Mach numbers. Bit Numer Math, 2005, 45(3): 463—480[DOI]
- 8 Klein R. Multiple spatial scales in engineering and atmospheric low Mach number flows. Esaim-Math Model Num, 2005, 39(3): 537— 559[DOI]
- 9 Roller S, Schwartzkopff T, Fortenbach R, et al. Calculation of low Mach number acoustics: A comparison of MPV, EIF and linearized Euler equations. Esaim-Math Model Num, 2005, 39(3): 561— 576[DOI]
- 10 Muller B. Low-Mach-number asymptotics of the Navier-Stokes equations. J Eng Math, 1998, 34(1-2): 97—109[DOI]
- Nerinckx K, Vierendeels J, Dick E. Mach-uniformity through the coupled pressure and temperature correction algorithm. J Comput Phys, 2005, 206(2): 597—623[DOI]
- 12 Turkel E. Preconditioned methods for solving the incompressible and low speed compressible equations. J Comput Phys, 1987, 72(2): 277—298[DOI]
- 13 Weiss J M, Smith W A. Preconditioning applied to variable and con-

- stant density flow. AIAA J, 1995, 33(11): 2050 2057[DOI]
- 14 Munz C D, Roller S, Klein R, et al. The extension of incompressible flow solvers to the weakly compressible regime. Comput Fluids, 2003, 32(2): 173-196[DOI]
- Schneider T, Botta N, Geratz K J, et al. Extension of finite volume compressible flow solvers to multi-dimensional, variable density zero Mach number flows. J Comput Phys, 1999, 155(2): 248—286[DOI]
- Schneider T, Botta N, Geratz K J, et al. Extension of finite volume compressible flow solvers to multi-dimensional, variable density zero Mach number flows. J Comput Phys, 2000, 158(2): 262-263[DOI]
- 17 Ghia U, Ghia K N, Shin C T. High-Re solutions for incompressible flow using the Navier-Stokes equations and a multigrid method. J Comput Phys, 1982, 48(3): 387—411[DOI]
- 18 Martí J M, Müller E. Numerical Hydrodynamics in Special Relativity, in Living Reviews in Relativity. Spain: Max Planck Institute for Gravitational Physics, 2003
- 19 Sod G A. A survey of several finite difference methods for systems of nonlinear hyperbolic conservation laws. J Comput Phys, 1978, 27(1): 1—31[DOI]
- 20 Huang J, Li R, He Y L, et al. Solutions for variable density low Mach number flows with a compressible pressure-based algorithm. Appl Therm Eng, 2007, 27(11-12): 2104—2112[DOI]
- 21 Du G H. Fundamental Acoustics (in Chinese). Nanjing: Nanjing University Press, 2001
- 22 Haydock D, Yeomans J M. Lattice Boltzmann simulations of attenuation-driven acoustic streaming. J Phys A: Math Gen, 2003, 36(20): 5683-5694[DOI]